ESTIMATION OF PETROPHYSICAL PROPERTIES OF TAR SANDS USING MICROTOMOGRAPHY

Caubit, C. (1), Sheppard, A.P. (2), Delottier L. (1), Hamon, G. (1).
(1) TOTAL (2) Australian National University

This paper was prepared for presentation at the International Symposium of the Society of Core Analysts held in Halifax, Nova Scotia, Canada, 4-7 October, 2010

ABSTRACT

Projects of thermal recovery processes in tar sands require the knowledge of several petrophysical properties, such as electrical properties for formation evaluation, or permeability and initial permeability to connate water for reservoir behaviour. This information can be acquired through conventional core measurements, often starting with extraction of the bitumen. However, suspicions exist about the validity of some petrophysical properties when measured once the solid hydrocarbon phase has been extracted. Another approach is proposed in this paper, which relies on micro computed tomography (micro-CT) and estimation of petrophysical properties through direct calculations, using the image of tar-saturated samples. This study was conducted in collaboration with the Australian National University (ANU). Six tar samples with two types of grain distribution were imaged. Image segmentation and simulation directly in the 3D images were performed to calculate petrophysical properties. These properties were compared with experimental data. The main conclusions of this investigation are the following: (1) Segmented images highlight that tar is located in smaller pores (2) Segmented images captured very well the porosity for the fine well sorted samples whereas they overestimated porosity for coarse poorly sorted rock (3) Segmented images capture very well the trend of the initial water saturation but overestimate it by approximately 12 Saturations Units compared to Dean Stark (considered as the reference value), (4) Formation Factor calculations in the 3D images are in very good agreement with the literature for unconsolidated samples (Humble's formula), (5) Resistivity Index calculations in the 3D images lead to Archie's coefficient greater than 2 and (6) Lattice Boltzmann calculations through the water phase volume for different subsets permit relative permeability estimation. We note that the water relative permeability can reach significant values even for high tar saturation due to the water location in the pore space.

INTRODUCTION

The microstructure of a porous medium, the physical characteristics of the solids and the fluids that occupy the pore space determine several macroscopic transport properties of the medium. One way to study this microstructure is through microtomographic imagery by X-ray facility, in which the pore space is reconstructed by acquiring a series of radiographs at different viewing angles over 360°. With this technique it is possible to determine the porosity (by segmentation) and the absolute permeability (by Lattice Boltzmann simulation) directly on the 3D images. In a previous paper [1] we have

demonstrated through a blind test that the algorithm elaborated by the Australian National University provided reliable predictions in terms of porosity and absolute permeability (k) for samples with low clay content, low microporosity fraction and with a k larger than 50mD. From these results we expect that the tar sand samples will be very good candidates for this technique because the clay content and microporosity are very limited and the anticipated permeability is larger than 1D. Moreover we are very interested in finding solutions to characterise tar sand because there are suspicions on laboratory results after bitumen extraction and/or coring and sampling as described by Dusseault et al. [2]. Dusseault highlighted also the influence of compaction on the measurement of permeability, this aspect will not be developed in this paper because in our case the porosity derived from Dean Stark and microtomography calculation are in very good agreement. As consequence, the samples can be considered as representative with a limited impact of the compaction.
So the major points of this investigation are the following:

- The special equipment used to take the tar sand samples and the procedures used to ensure that representative samples are imaged.
- The main characteristics of the micro-CT equipment, as well as the processing of the images, which was performed to minimise all image artefacts
- The images of tar sand samples. The location of the bitumen within the pore network is illustrated.
- The values of porosity derived from the micro tomography images, two different sources conventional core data (Dean Stark and after bitumen extraction) and the logs are compared. Uncertainties in the conventional laboratory methods as well as segmentation issues for images are discussed. Differences in estimations through microtomography for fine well sorted and coarse, poorly sorted rocks are illustrated.
- The comparison between the initial water saturation from the micro tomography images, two different laboratory methods and logs is presented. Uncertainties are discussed.
- The calculated permeability, formation factor, resistivity index and water-oil relative permeability curves are presented. The impact of electrical parameters on the water saturation is investigated through a log interpretation with Archie's law.

MATERIALS AND PROCEDURE USED FOR SAMPLING

The sampling process is a key point for our study: the main difficulty is in finding a method for the extraction of tiny cylindrical samples (6mm in diameter and 2-4cm in length) without creating any porous media disturbance and with the possibility of axial-stress application during shipping or before imaging. To ensure transparency to the micro-CT scan, the sample is conditioned in a thin-walled 10 cm long beveled aluminum tube. The samples are extracted by a core punching method. This method consists of introducing the aluminum tube by hand directly into the tar sand with a system designed to allow movement in only one direction, perpendicular to the slabbed core (Figure 1a &

b). Once the aluminum tube reaches the core barrel, the tube is turned softly to cut the core and to minimize core expansion or air gap creation during extraction.

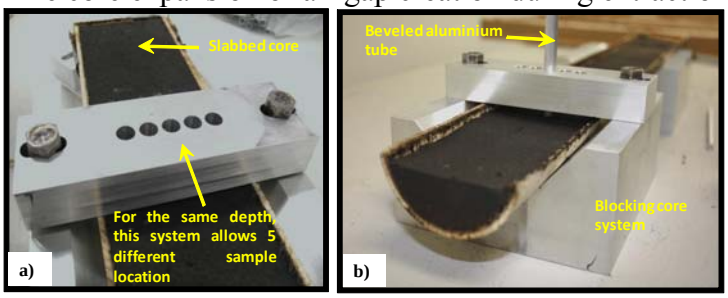

Figure 1: a) Punching system b) blocking system

From now on, the sample remains in its beveled aluminum tube but must be conditioned carefully to avoid porous media expansion during transport. Therefore the beveled extremity of the tube is closed by the introduction of an aluminum cap which is blocked by slightly reducing the tube diameter at the extremity as shown Figure 2a & b.

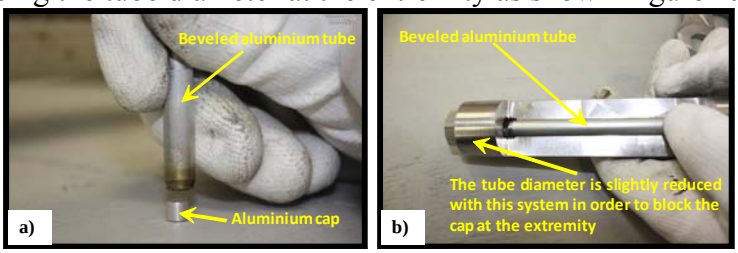

Figure 2: a) Cap positioning b) Cap sealing

The axial stress application system is located at the second extremity. A full diameter aluminum cylinder is introduced into the aluminum tube to constrain the sample. Once the cylinder reaches the bitumen sand, a nut is added to lock the cylinder and the tube together. Consequently, the sample is well-conditioned and cannot move or expand during shipping, as shown Figure 3a. If necessary, the axial loading might be evaluated and adjusted by the use of a strength gauge combined with an indicator as described Figure 3b.

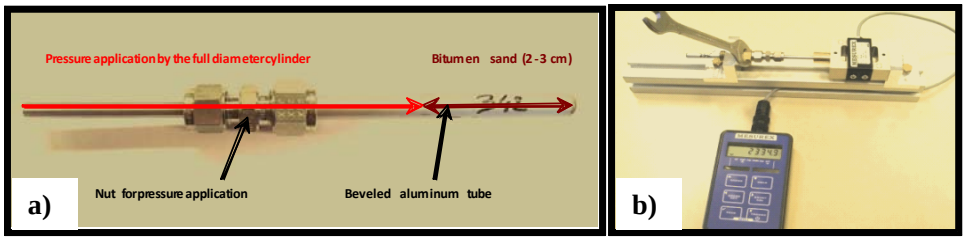

Figure 3: a) Shipped samples b) Device to assess the axial stress

With this technique 38 plugs were sampled on cores impregnated with tar from a unconsolidated reservoir. Then 6 samples were selected after verification of the sample integrity with in-house CT scanner. Finally, these samples (labeled 210, 242, 262, 332, 341 & 343) were imaged with microtomograph. It is worth noting that the cores were unpreserved and it was very difficult to obtain samples without any disturbance.

MICROTOMOGRAPHIC DEVICE AND IMAGE PROCESSING

Microtomographic device:

Figure 4 displays the X-ray micro-CT facility with a cone beam geometry designed by ANU. Normally this device is used to image consolidated rock free of reservoir fluids. Our study is more complex because we try to image a sand which is impregnated with tar. Indeed it is very difficult to discriminate the tar from the other materials present since without being doped with a contrast agent, tar weakly attenuates the 40-80keV X-rays used in the experiments, so there is little contrast between the tar and air. Therefore, in order to accurately identify the porosity and the fluid saturation it is necessary that the tomographic acquisition and the subsequent processing steps be highly optimised. For these samples, a resolution of 5 microns was required. High X-ray flux and 5 micron spot size are achieved using a microfocus X-ray tube with a tungsten reflection-style target. Detection of individual X-ray photons is achieved with a 130µm CsI scintillator coupled via an optic fiber taper to a high-capacity military grade 4 megapixel CCD camera, cooled to -35 degC [3, 4, 5].

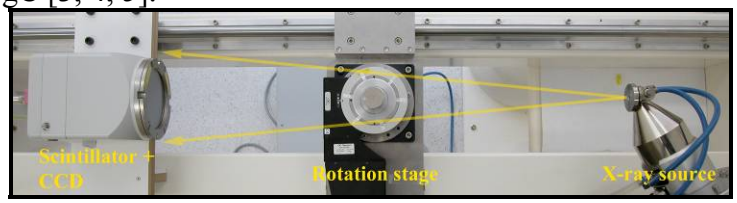

Figure 4: Illustration of the X-ray facility with a core sample placed on the rotation stage

Image processing: results on tar sands

The quality of the tomographic acquisition is maximised through the longest practical acquisition time, in this case over 24 hours. Any thermal drift that may occur during this time is removed using a key-field alignment process, and geometric alignment errors are compensated for by an iterative reconstruction technique that maximises image contrast. This results in a sharp tomographic image containing 8 billion voxels and with a very high signal-to-noise ratio (SNR). Even with images of this quality, accurate discrimination of the phases from one another demands careful analysis. The SNR is improved by using a custom anisotropic diffusion edge-preserving noise reduction filter [6]. After the image acquisition and processing, grey-scale images are obtained highlighting two different types of sample: (1) fine and well sorted (Figure 5) and (2) coarse poorly sorted (Figure 6). The quality of the images is very good allowing clear visual discrimination of the three phases in the samples (i.e. grain, tar and void). Indeed, in the images, there are black region, dark grey region and light grey representing respectively the void, the tar and the grain. This result confirms our preliminary hypothesis that the water content has evaporated during storage. As far as sample integrity is concerned, no major disturbance related to the sampling was observed. This result is encouraging and allows confidence in the representativeness of the sample. Moreover this observation was confirmed by radial and axial porosity measurement. In the radial direction the porosity remains constant in the center whereas a large local increase is noted (15 Porosity Units) at the side of the aluminum tube due to the sampling procedure. Axially a porosity gradient is observed (3 P.U. of variation) which can be

attributed to the axial stress applied with our device of sampling. All these observations suggest that the segmentation and the calculation have to be performed on subsets in the centre of images. All the data regarding the segmentation are gathered in the next section.

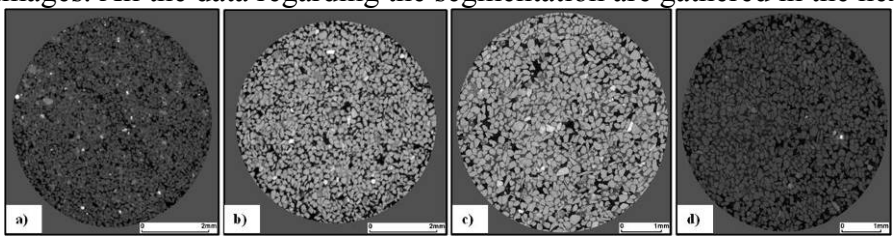

Figure 5: Fine and well sorted samples a) #210, b) #242, c) #262 and d) #332.

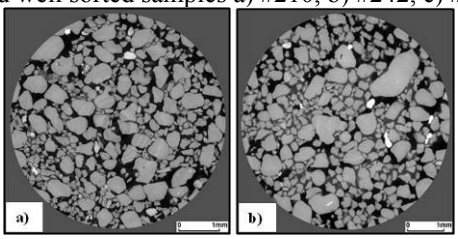

Figure 6: Coarse and poorly sorted samples a) #341 and b) #343.

SEGMENTATION RESULTS AND COMPARISON WITH EXPERIMENTAL DATA

Three-phase segmentation: phase separation and location

To accurately segment the three phases (solid, tar and air) from one another, we use a seeded region-growing method where growth rate depends on the local gradient and interface advance is calculated using the fast marching method [7]. To enable these sophisticated techniques to be used on such large data sets, all image analysis methods are implemented for distributed-memory parallel computer architecture. Classically this segmentation technique is used for two-phase material implying a two-level thresholding to initialize the algorithm. In our case the situation is more complex and requires a four-level thresholding due to the shape of the intensity distribution with different peaks corresponding to the void, the tar and the grain (Figure 7b). After this image processing we obtained the segmented image (Figure 7c) with in black the void, orange the tar and in white the grain. The quality of segmentation seems excellent even if isolated discrepancies can be observed as shown in the red ellipse in Figure 7a & c. Indeed several grains visible in the grey-scale image are not resolved in the segmented image. Nevertheless, experience at ANU suggests that the impact on porosity and saturation calculations are limited to 2% over the whole volume. Another point which can impact the saturation and porosity is the beam hardening. For our samples, this effect is minimized by filtering the beam with silica, and by the aluminum tube. In addition, our region-growing segmentation method uses image gradient to find phase boundaries and is therefore relatively insensitive to an overall shift in intensity limiting the impact on the saturation. Finally the main information which can be drawn from segmented images without calculation is the phase location. Indeed, in the Figure 7c, we note that the tar fills mainly the smaller pores. This observation is contradictory with classical theory regarding the pore occupancy during a primary drainage in strongly water wet condition.

Research on this topic is still ongoing, we try to confirm and explain the bitumen location thanks to an ESEM study.

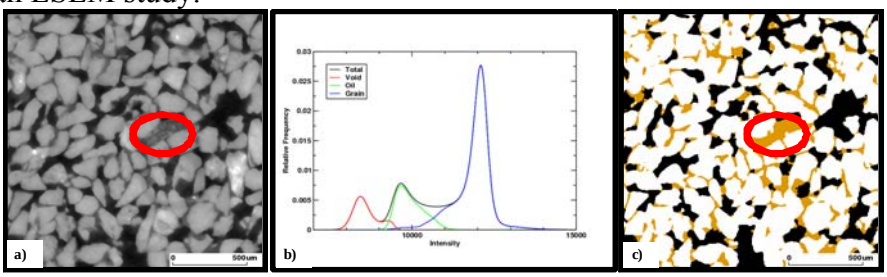

Figure 7: Segmentation process a) Grey scale image, b) Intensity distribution & c) Segmented image

Porosity results:

The Figure 8a presents a comparison between the porosity calculated on segmented images and the porosity measured by Dean Stark (DS) extraction (carried out immediately after coring) and logs at the same reservoir depth. It is worth noticing that the porosities derived from the interpretation of porosity Logs is matched on the DS values therefore the most reliable data for porosity is DS. Moreover the absolute porosity errors (µTomo vs Logs and µTomo vs DS) are plotted in the Figure 8b. We note: 1) a very good agreement between µTomo and DS porosity for the fine well sorted samples (#210, #242, #262 & #332) whereas the segmented porosity overestimates the DS value from 2.3 to 4.1 PU for the coarse poorly sorted rocks (#341 & #343), 2) Uncertainty on DS porosity is accurate to 0.01 PU which cannot explain this discrepancy in the coarse grained samples. Two conclusions can be drawn to explain this discrepancy (1) a lack of representativity of sample due to insufficient volume for this coarse, poorly sorted type of samples, (2) excessive disturbance due to the sampling procedure.

Moreover we note a very poor agreement between porosity derived from saturation measured during DS tests and the bulk porosity measured after bitumen extraction the plugs as shown in the Figure 8a for the sample #210 and # 242. The discrepancy between the two techniques is around 10% which can have a big impact on saturation. Consequently, it suggests that the bulk porosity measurement after tar extraction provides unreliable data. In the next section we will focus our attention on the water saturation determined by different methods.

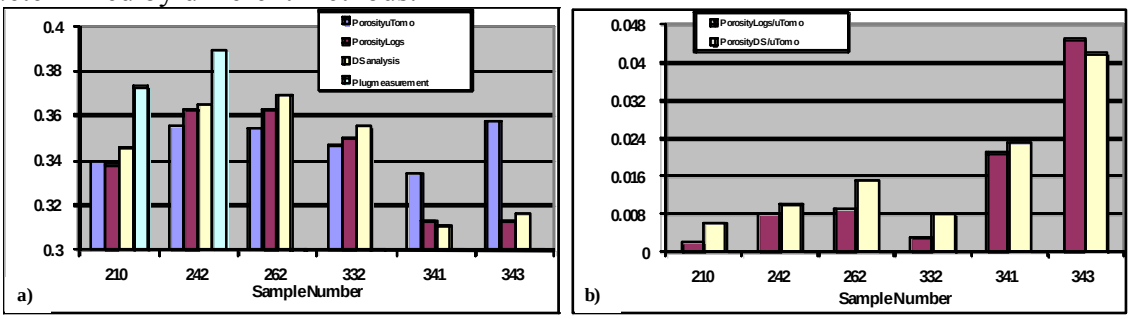

Figure 8: a) Comparison in terms of porosity between µTomo, Logs, DS & Plugs b) Porosity absolute error Logs vs µTomo & DS vs µTomo.

Initial water saturation results: Comparison with in-house data

In this section the samples with unreliable results in terms of porosity have been discarded (i.e. #341 & #343).

Comparison with Logs data & Dean stark measurements:

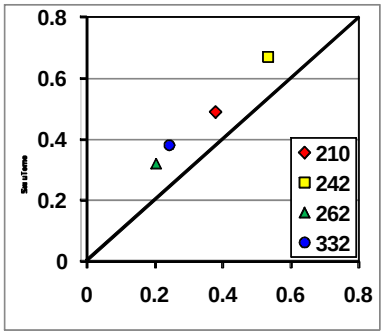

The Figure 9a displays all the results in terms of water saturation (i.e. µTomo segmentation, Logs and DS measurements). As previously the saturation logs are matched on the DS values therefore the most reliable information lies in the DS measurement. We note: 1) The trend in saturation is well captured as shown on the figure on the right 2) The water saturation derived from segmented images overestimates the DS value by 12 saturation units (SU) as shown Figure 9b. The uncertainty of DS measurement is estimated to be below 0.2 SU for classical samples and cannot explain the discrepancy. To confirm this result we decided to perform a new measurement directly used for microtomography imaging with another technique called Accelerated Solvent Extraction (ASE) [8], particularly adapted to tiny samples. All the results regarding the ASE measurements are gathered in the next section.

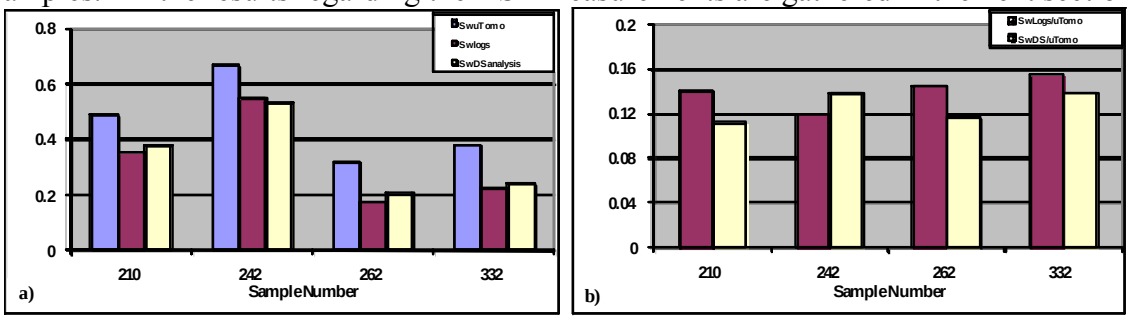

Figure 9: a) Comparison in terms of water saturation between µTomo, Logs and DS b) Water saturation absolute error Logs vs µTomo and DS vs µTomo.

Comparison with Accelerated Solvent Extraction (ASE):

Three samples have been selected to undergo an ASE measurement (i.e. #210, #242 & #262). The method consists of extracting the organic and the water phase by injection of solvent (Dichloromethane) in pressure (100 bars) and temperature (100°C). Then the aqueous phase and the solvent are respectively removed by filtration with hydrophobic filter and evaporation in a water bath. With this technique we have determined the mass of tar, water and rock as shown in the Table 1. The very low extracted mass of water confirms that the initial water content was almost totally evaporated during core storage. As a consequence the water saturation was calculated using the DS porosity and assuming that the pore volume is fully saturated with water and tar at reservoir condition. Water saturations derived from ASE data are completely in line with the DS values (Figure 10), confirming that image segmentation overestimates the DS value. No reasonable hypothesis was found to explain this issue. The error on the phase volume inherent to the segmentation is estimate to be around 2% which is not sufficient to justify

the water saturation discrepancy. The next section presents petrophysical properties calculated directly in the 3D images.

Sample#	Bitumen mass (mg)	Water mass (mg)	Rock mass (mg)
210	152	9.6	1259.4
242	121.1	13.8	1202.8
262	205.6	19.3	1227.2

Table 1: Water, oil and rock mass determined by the ASE measurement

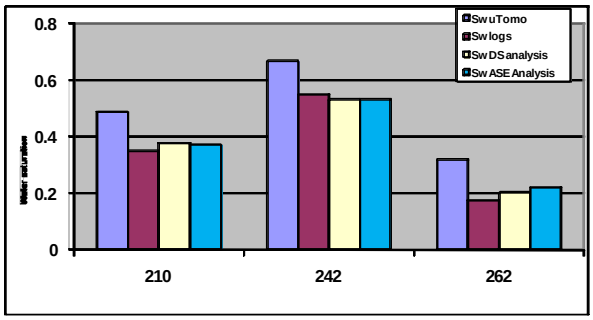

Figure 10: Comparison of the water saturation derived from ASE data with **μTomo**, Logs and DS results

CALCULATION OF PETROPHYSICAL PROPERTIES

In this section all the results concern only the fine grain samples that have a reliable value of porosity compared to the log data (i.e. samples# 210, 242, 262 and 332). Moreover the calculations regarding the electrical properties, the absolute permeability and the Bitumen/Water relative permeability have been performed in three orthogonal directions on two subsets of 840^3 voxels and several smaller subsets (280^3 & 420^3 voxels).

Electrical properties

The formation factor (FF) and resistivity index (RI) calculation is based on a solution of the Laplace equation with charge conservation boundary conditions using a conjugate gradient technique [9]. For the formation factor calculation an idealized case was considered, assigning zero conductivity to all mineral phases. For the resistivity index calculation both the non-wetting phase and the mineral phase are assumed to be non-conductive. Water is the only conductive phase and the water films are not considered. The Figure 11 exhibits all the results in terms of evolution of the FF as a function of the porosity. The Table 2 exhibits the parameters extracted from the two following models: $FF=1/\Phi^{mbest}$ and $FF=a/\Phi^{m}$. These data are globally in very good agreement with the "Humble formula" defined by $FF=0.62/\Phi^{2.15}$ for unconsolidated samples [10].

Sample #	m_{best}	a	m
210	1.69	0.51	2.25
242	1.65	0.66	2
262	1.58	0.82	1.8
332	1.6	0.63	2

Table 2: Parameters for two different formation factor models.

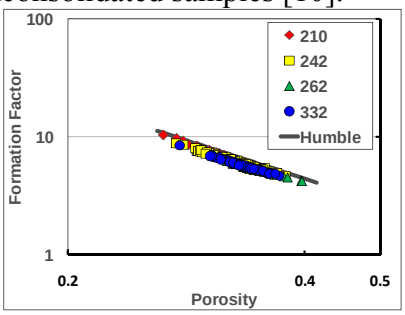

Figure 11: Formation factor vs porosity for different subsets of the 3D images (log-log scale).

The simulated resistivity index for each sample is plotted in the Figure 12 as function of the water saturation. We observe a non linear behavior with a significant increase of the

resistivity for the low water saturation. Wei et al. [11] describe similar results during an oil injection in oil-wet sand. The hypothesis of wettability to oil is in line with the phase location observed on segmented (i.e. water in the larger pores and oil in the smaller pores). The Table 3 gathers the parameters derived from the following resistivity index models: $RI=1/Sw^{nbest}$ and $RI=b/Sw^{n}$. We note that the Archie's coefficient n_{best} is significantly greater than 2. This result can be attributed to the water location which is in the larger pores.

Sample #	n_{best}	b	n
210	4.2	0.24	5.5
242	5.1	0.24	6.9
262	2.9	1.9	2.5
332	3	1.1	3

Table 3: Parameters for two different resistivity index models.

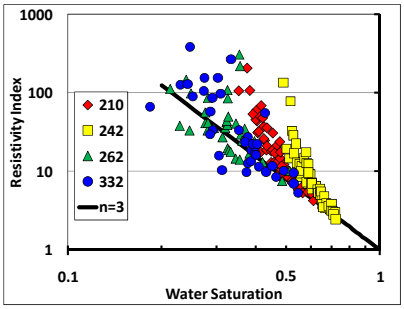

Figure 12: Resistivity index vs water saturation for different subsets of the 3D images (log-log scale).

In the Figure 13 we derived the water saturation from classical log interpretation with the Archie's law defined by the following equation: $Sw = \sqrt[n]{a\Phi^{-m} Rw / Rt}$. With this equation we have tested the frequently used electrical parameters used for unconsolidated sample (i.e. a= 1, m=1.55 and n=2) and those derived from calculation on the 3D images for the sample #210, #242 & #262. It is worth noticing that these three samples were selected in the same well at three different depths. Therefore the Rt values presented in the Table 4 were picked from the resistivity logs at the depth of each sample. Two values of Rw (Table 4) were determined for two salinities corresponding to the maximum and minimum values encountered in the field. With all these parameters the water saturation were calculated for each case. On the one hand we note that water saturations determined with the tomographic derived electrical parameters overestimates systematically the DS value but remain coherent with the segmented values (Figure 13). On the other hand the water saturation estimated with the classical electrical parameters is in good agreement with the DS for the sample #242 and #262 whereas we note a large discrepancy for the sample #210 as shown in the Figure 13.

Sample#	210	242	262
$Rw_{HighSal}$ (Ω)	0.82	0.82	0.82
Rw_{LowSal} (Ω)	1.2	1.2	1.2
Rt (Ω)	95.5	25.5	139.2

Table 4: Formation resistivity, Water resistivity for high and low salinity.

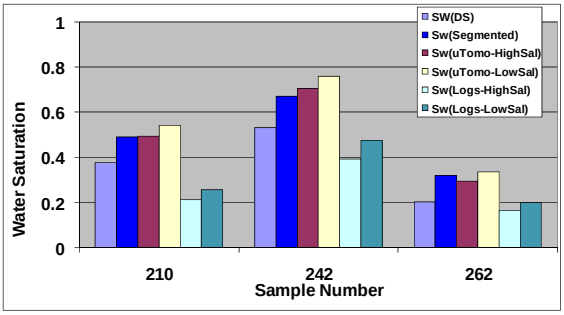

Figure 13: Water saturation calculated with electrical parameters derived classical logs interpretation or ANU method.

Single phase properties: Absolute permeability

The absolute permeability calculation is based on the lattice-Boltzmann method (LB) [12] The LB approach is a mesoscopic numerical method used in computational fluid dynamics, where the macroscopic dynamics of the solution of a discretized Boltzmann equation can be shown to match the Navier-Stokes equation. Due to its simplicity in form and adaptability to complex flow geometries, like the presence of solid-fluid boundaries, one of the most successful applications of the LB method has been to flow in porous media. The LB method was used to solve for the pressure drop along the image for a fixed flow rate and calculate k in the conventional manner. The Table 5 presents the absolute permeabilites calculated directly in the 3D images by the LB method. We have no experimental results regarding these samples nevertheless we can be confident on these values because we have demonstrated in a previous study [1] that the uncertainty on k calculated by LB method without any calibration was less than 40%. This uncertainty concerns only the clean samples with limited microporosity, which is the case for our tar samples.

Sample#	210	242	262	332
K(D)	3.38	6.66	10	7.13

Table 5: Absolute permeability results

Multiphase flow properties: Water relative permeability

Water relative permeability:

The water relative permeabilities are calculated directly in the 3D image using LB method as described previously. Water effective permeabilities are not calculated on the whole pore volume as the absolute permeability but only through the phase volume (water) on several subsets with different saturation states. Then the absolute permeability is used as reference to determine the relative permeability. With this technique we are able to describe the water relative permeability on a large range of saturation as shown on the Figure 14. We note that the water relative permeability can reach a significant value even for high tar saturation. This result can be attributed to the water location. Indeed the water fills the larger pores leading to high conductivity and relative permeability at a given saturation. The information is very interesting in term of thermal processes because it suggests a large water injectivity. Currently we did not plan to compare these results with experimental relative permeability because in our opinion experiments performed on samples which have undergone bitumen extraction are not reliable.

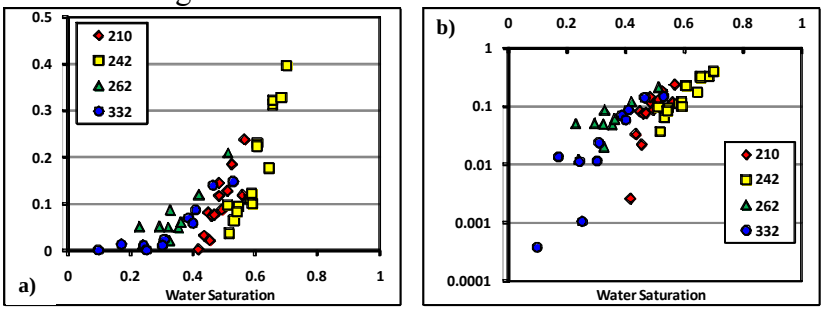

Figure 14: Water relative permeabilities a) Linear scale b) logs scale

CONCLUSIONS

The main conclusions of this paper are the following:

- Robust sampling procedure was designed to minimize disturbances which is crucial for microtomographic imagery.
- Major improvements of the imaging device (thermal drift and alignment compensation algorithm) allow acquisition of sharp microtomographic images. These images show no major disturbance for all the samples.
- Segmented images highlight that tar is located in smaller pores.
- Segmented images captured very well the porosity for the fine well sorted samples whereas they overestimated porosity for coarse poorly sorted rock.
- Segmented images capture very well the trend of the initial water saturation but overestimate it by approximately 12 Saturations Units compared to Dean Stark (considered as the reference value). No convincing explanation was found to justify this discrepancy.
- FF calculations in the 3D images are in very good agreement with the literature for unconsolidated samples (Humble's formula).
- RI calculations in the 3D images lead to Archie's coefficient greater than 2.
- Calculations in the 3D images provide absolute permeabilities which are consistent with laboratory results.
- LB calculation through the water phase volume for different subsets permit the estimation of the effective water permeability at the initial water saturation with an uncertainty around 40%. We note that the water relative permeability can reach significant values even for high tar saturation due to the water location in the pore space.

We are continuing to work on this topic and the major points of the way forward are the following:

- More investigations to uncover the cause of discrepancy between the water saturation values calculated from microtomographic images and the values derived from experimental methods such as DS and ASE;
- Investigate the 3D topology of the tar phase in order to understand if the tar location is due to wettability or pore accessibility issues.
- Injections of contrast fluid are scheduled in order to improve the quality of water phase estimation by segmentation.

ACKNOWLEDGEMENTS

We wish to thank Total for giving its permission to publish this work. We are also especially grateful to the Australian National University Department of Applied Mathematics for work carried out.

REFERENCES

1. Caubit, C., Hamon, G., Sheppard, A.P., Øren, P. E., Evaluation of the reliability of petrophysical data through imagery and pore network modeling *Proceedings of the Annual Symposium of the Society of Core Analysts held in Abu Dhabi*, SCA2008-33 (2008).
2. Dusseault M.B. and Scott J.D., Coring and Sampling in heavy-oil exploration: Difficulties nad proposed solution *Exploration methods*, Section IV, (1987) 437-442
3. Sakellariou, A., Senden, T. J., Sawkins, T. J., Knackstedt, M. A., Turner, M. L., Jones, A. C., Saadatfar, M., Roberts, R. J., Limaye, A., Arns, C. H., Sheppard, A. P., Sok, R. M.., An x-ray tomography facility for quantitative prediction of mechanical and transport properties in geological, biological, and synthetic systems: *Development in X-Ray Tomography IV* (2004): 473–484.
4. Sakellariou, A., Arns, C. H., Limaye, A., Senden, T. J., Sheppard, A. P., Sok, R. M., Pinczewski, W. V., Knackstedt, M. A., Berge, L., and Øren, P., μ-ct facility for imaging reservoir rocks at pore scales: μ-ct facility for imaging reservoir rocks at pore scales, *SEG Technical Program* (October 2003)
5. Sakellariou, A., Sawkins, T. J., Senden, T. J., and Limaye, A., X-ray tomography for mesoscale physics applications: *Physica A*, 339, (2004a) 152–158.
6. Frangakis A.S. and Hegerl R., Noise reduction in electron tomographic reconstructions using nonlinear anisotropic diffusion, *Journal of Structural Biology* 135, no. 3 (2001): 239–250.
7. Sheppard A; P., Sok R. M., and Averdunk H., "Techniques for image enhancement and segmentation of tomographic images of porous materials," *Physica A: Statistical Mechanics and its Applications* 339, no. 1-2 (2004): 145–151.
8. Richter B. E., Jones B. A. Ezzell J. L., Porter N. L. Avadalovic N. and Pohl C. Accelerated solvent Extraction: A technique for sample preparation, *Analytical Chemistry*, 68 (1996), 1033-1039
9. Arns, C. H., Knackstedt, M. A., Pinczewski, W. V., and Lindquist, W. B., Accurate computation of transport properties from microtomographic images: *Geophysical Research Letters*, 28, (2001), 3361–3364.
10. Winsauer W. O., Shearin H. M., Masson P. H., Williams M., Resistivity of Brine-Saturated Sands in Relation to Pore Geometry, *AAPG Bulletin,* Vol. 36, Issue 2, (1952), 253-277
11. Wei J-Z and Lile O. B., Hysteresis of the resistivity index in unconsolidated porous medium *Proceedings of the Annual Symposium of the Society of Core Analysts*, SCA9212 (1992).
12. Martys, N. S., and Chen, H., 1996, Simulation of multicomponent fluids in complex three-dimensional geometries by the lattice Boltzmann method: *Phys. Rev.* E, 53, (1996) 743–750.